



THE UNIVERSITY *of* EDINBURGH

Edinburgh Research Explorer

A combined rheometry and imaging study of viscosity reduction in bacterial suspensions

Citation for published version:

Martinez, VA, Clement, E, Arlt, J, Douarche, C, Dawson, A, Schwarz-Linek, J, Creppy, AK, Skultety, V, Morozov, A, Auradou, H & Poon, W 2020, 'A combined rheometry and imaging study of viscosity reduction in bacterial suspensions', *Proceedings of the National Academy of Sciences (PNAS)*, vol. 117, no. 5, pp. 2326-2331. <https://doi.org/10.1073/pnas.1912690117>

Digital Object Identifier (DOI):

[10.1073/pnas.1912690117](https://doi.org/10.1073/pnas.1912690117)

Link:

[Link to publication record in Edinburgh Research Explorer](#)

Document Version:

Peer reviewed version

Published In:

Proceedings of the National Academy of Sciences (PNAS)

General rights

Copyright for the publications made accessible via the Edinburgh Research Explorer is retained by the author(s) and / or other copyright owners and it is a condition of accessing these publications that users recognise and abide by the legal requirements associated with these rights.

Take down policy

The University of Edinburgh has made every reasonable effort to ensure that Edinburgh Research Explorer content complies with UK legislation. If you believe that the public display of this file breaches copyright please contact openaccess@ed.ac.uk providing details, and we will remove access to the work immediately and investigate your claim.



A combined rheometry and imaging study of viscosity reduction in bacterial suspensions

Vincent A. Martinez^{a,1,2}, Eric Clément^{b,1,2}, Jochen Arlt^a, Carine Douarche^c, Angela Dawson^a, Jana Schwarz-Linek^a, Adama K. Creppy^c, Viktor Škultétý^a, Alexander N. Morozov^a, Harold Auradou^c, and Wilson C. K. Poon^a

^aSUPA and School of Physics & Astronomy, The University of Edinburgh, Edinburgh EH9 3FD, United Kingdom.; ^bPhysique et Mécanique des Milieux Hétérogènes (UMR 7636 ESPCI/CNRS/Université P.M. Curie/Université Paris-Diderot), 10 rue Vauquelin, 75005 Paris, France.; ^cLaboratoire FAST, Univ. Paris-Sud, CNRS, Université Paris-Saclay, F-91405, Orsay, France.

This manuscript was compiled on November 21, 2019

Suspending self-propelled ‘pushers’ in a liquid lowers its viscosity. We study how this phenomenon depends on system size in bacterial suspensions using bulk rheometry and particle-tracking rheoimaging. Above the critical bacterial volume fraction needed to decrease the viscosity to zero, $\phi_c \approx 0.75\%$, large-scale collective motion emerges in the quiescent state and the flow becomes non-linear. We confirm a theoretical prediction that such instability should be suppressed by confinement. Our results also show that a recent application of active liquid crystal theory to such systems is untenable.

Escherichia coli | rheology and imaging | particle tracking | particle image velocimetry | Active Matter |

Suspensions of self-propelled particles (1) show surprising properties due to time-reversal symmetry breaking (2, 3) and the unique flow fields associated with self-propulsion (4). Different classes of self-propelled particles exist, differing in the symmetry of these flows (5). A motile *Escherichia coli* bacterium propelling itself using a helical flagellar bundle powered by rotary motors is a ‘pusher’. *Chlamydomonas* algae, which swim by beating two flagella at the front of each cell, are ‘pullers’. The symmetries of the corresponding flow fields have a definite influence on the ability to generate collective motion: at sufficiently high concentration, but still rather dilute, suspensions of pusher swimmers exhibit orientational instabilities and collective motion, while suspensions of pullers remain stable (6, 7).

In an external flow field, the presence of shear influences greatly the average swimming orientations and consequently the stress generated by the micro-swimmers (8). For a suspension of pushers at low-shear, hydrodynamic theories predict an alignment of the swimming direction. This enhances the applied shear stress and leads to a apparent viscosity that decreases with increasing volume fraction of cell bodies, ϕ , i.e. a negative viscosity increment (NVI). Symmetry again holds the key: pullers are not predicted to show NVI, and indeed a positive viscosity increment was found in *Chlamydomonas* suspensions using cone-plate rheometry (9). For pushers, NVI was inferred in *Bacillus subtilis* in non-rheometric geometries (10), and directly measured for *E. coli* in a microfluidic rheometer (11, 12) and in a cylindrical Couette geometry (13). Throughout this work, viscosity refers to a global rheological measure of sample’s properties (sometimes known as the ‘apparent viscosity’); the local viscosity experienced by a bacterium is equal to the viscosity of the surround aqueous medium under all conditions: the drag from this unchanged local viscosity remains the source of flagellar propulsion.

These advances notwithstanding, bacterial NVI is far from understood. In particular, the so-called ‘superfluidity regime’

of vanishing and then negative effective viscosity (13) predicted by theory (14) remains mysterious. Indirect observations imply a possible connection with the emergence of large-scale collective motion (15). The latter is expected by continuum kinetic theory to be strongly affected by confinement (16, 17). Separately, a recent application of active liquid crystal theory to NVI implies that this phenomenon should be strongly system-size dependent (18).

System size dependence is long known and substantially understood in equilibrium phase transitions near critical points (19) and in kinetically-arrested materials such as polymer films (20). These bodies of work show that probing system-size effects can generate new fundamental insights, e.g., into the putative role of divergent length scales.

Size dependence has often been suggested for active matter. For example, the effect of confinement on the flocking transition in the Vicsek model has long been debated. Recent simulations find that this transition disappears when boundaries are removed, but is recovered for scale-free interactions (21). Theories predict a variety of size-dependent effects in other active systems (see (22) and refs inside). However, these predictions, including ones concerning NVI and collective motion, have seldom been experimentally probed, so that the relevance of many results from theory and simulations remains

Significance Statement

A pot of paint is more viscous than water due to many ‘bits and pieces’ suspended in paint, such as pigment particles. Amazingly, the viscosity of a dilute suspension of swimming bacteria has been found to be *lower* than that of water. A number of theories claim to explain this effect. We test a crucial prediction of one of these theories, viz., that the strange viscosity reduction should be strongly dependent on the system-size in which the measurements are made. Such strong size-dependence was not observed. Instead, we find direct evidence that when the viscosity of the bacterial suspension is reduced to near zero, the swimming microbes begin to ‘swarm’ in a way reminiscent of flocking in birds or fish.

V.A.M., E.C., W.C.K.P. initiated the work; V.A.M., E.C., J.A., C.D. performed the rheo-imaging experiments in Edinburgh; V.A.M., E.C., J.A., C.D., A.C., H.A. performed the rheology experiments in Orsay; V.A.M., E.C., J.A., C.D. analysed the data; J.S-L and A.D. elaborated the sample growth protocols; V.A.M., C.D., A.D. J.S-L prepared the samples; A.D. created the AD21 strain; A.N.M. and V.S. provided theoretical insights; V.A.M., E.C., A.N.M. and W.C.K.P. wrote the paper; All authors participated to the scientific discussions and provided comments at the writing stage.

The authors declare no competing interests.

¹ V.A.M. and E.C. contributed equally to this work.

² To whom correspondence should be addressed. E-mail: vincent.martinez@ed.ac.uk, eric.clement@upmc.fr

to be demonstrated.

In this work, we study the size dependence of NVI by varying the gap size of the Couette rheometer (13) used to measure the viscosity of bacterial suspensions. At the same time, we imaged the same samples in a cone-plate rheometer (23) to investigate the link to collective motion. Our results show that a recent application of active liquid crystal theory to bacterial suspensions is untenable, uncover a direct connection between NVI and collective motion, and confirm continuum kinetic theoretic predictions of the latter's size dependence. Our findings give a firm basis for developing more adequate theories for one of the most striking phenomena in active matter physics. Below, we first review current theories for NVI and collective motion, focussing on what they have to say about size dependence, before reporting our results.

Current theories

There are two main current theories (22) for bacterial NVI: continuum kinetic theory (CKT) of dilute active suspensions, and active liquid crystal theory (ALCT) developed to describe active systems with underlying nematic order such as dense microtubule solutions driven by kinesin motors (24). Both theories have recently been applied to sheared bacterial suspensions (7, 18, 25–27).

ALCT applied to *any* system predicts a strong size dependence traceable back to a bending elasticity term in the description of the energetics of all liquid crystals. Passive microtubule bundles form a nematic liquid crystal (LC). With sufficient motor activity, the system develops spontaneous flow, which can be modelled (22) by adding an active stress term to the equations of (passive) nematohydrodynamics (28). The active stress competes against the LC's bending elasticity, which has energy density $u_b = \frac{1}{2} K [\mathbf{n} \times (\nabla \times \mathbf{n})]^2$, where \mathbf{n} is the nematic director and K is a Frank elastic constant (29). Between parallel plates separated by H with parallel ordering at the plates, $u_b \sim K/H^2$. An H^2 dependence permeates the theory, reflecting the centrality of orientational elasticity. Importantly, the active stress required to set up spontaneous flow without external driving also scales as H^{-2} .

This theory was recently adapted for the rheology of dense bacterial suspensions (18). As expected, all of its results show size dependence. For example, the theory implies a strong enhancement with system-size of the critical shear rate $\dot{\gamma}_c$ above which NVI disappears (13). In a suspension viscosity η , tumbling of the director commencing at $\eta\dot{\gamma} \sim K/H^2$ suppresses NVI, so that

$$\dot{\gamma}_c \sim K/\eta H^2. \quad [1]$$

Elasticity also determines the form of the ALCT viscosity (18):

$$\eta \approx \eta_0 [1 - \beta(KH^{-2})^{-1}], \quad [2]$$

where β depends on the activity and η_0 is the solvent viscosity. ALCT also predicts non-linear flow profiles associated with the emergence of NVI. ‘Shear banding’ has indeed been observed recently in bacterial suspensions, although the link with NVI was implied rather than directly established (15).

Mean-field CKT (7, 25–27), formulated in terms of the probability distribution function of the swimmer positions and orientations, treats pushers as moving force dipoles. Without external flow, it predicts that homogeneous and isotropic

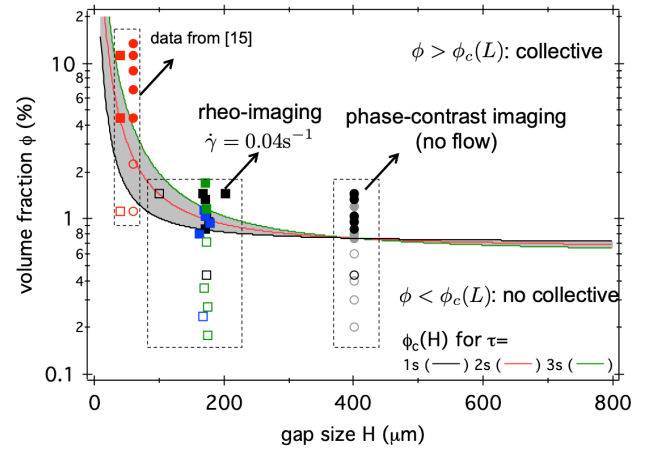


Fig. 1. Confinement effect on flow stability and collective motion. Lines: calculated confined critical volume fraction $\phi_c(H)$, according to continuum kinetic theory using Eq. 4 and the experimentally measured $\phi_c(H = 400 \mu\text{m}) \approx 0.75\%$ (see Figure 4(i-j)) as ϕ_c^∞ . $\phi_c(H)$ defines the boundary between stable (below) and unstable (above) pusher suspensions for different persistence time τ of the swimmers as indicated in the legend with speed $v = 15 \mu\text{m s}^{-1}$. Symbols: experimental observation of flow with (filled squares) and without (open squares) banding; and with (filled circles) or without (open circles) large correlation length-scale l , based on rheo-imaging (squares) and phase-contrast imaging (no flow, circles) respectively. See Figure 4 and related main text for more details. Red: data extracted from (15) at $H = 60 \mu\text{m}$ (an x -offset is applied to squares for better visualisation).

configurations of infinite systems are linearly unstable above a swimmer volume fraction ϕ_c^∞ . It is usually thought that this constitutes the threshold for collective motion, although large-scale 3D simulations show a less clear-cut picture (30). Under simple shear, CKT was adapted and a mean-field Smoluchowski equation solved (27) for straight swimmers undergoing rotational diffusion, yielding a low-shear rate prediction of the viscosity of the suspension. Keeping only the relevant ‘active’ contribution and replacing rotational diffusion with tumbling, relevant for our work, we arrive at

$$\frac{\eta}{\eta_0} = 1 - \frac{\phi}{\phi_c^\infty}. \quad [3]$$

This result intimately relates vanishing shear viscosity to the onset of collective motion, albeit only in infinite systems: CKT treats the driving flow as homogeneous and infinite, and is thus insensitive to the size of the system. Moreover, with few exceptions (31, 32), CKT studies of rheology to date have ignored inter-particle interactions.

Formulating a CKT in confinement properly is technically demanding. However the infinite-system results can be used to estimate how the instability threshold should depend on H . The linear stability analysis of infinite systems gives the dependence of the instability eigenvalue on the perturbation wavelength k (16, 27). The most unstable mode is predicted to occur at $k = 0$, so that ϕ_c^∞ is the critical volume fraction. To estimate the confined critical volume fraction $\phi_c(H)$, we set the largest available scale to $k = 2\pi/H$, giving

$$\frac{\phi_c(H)}{\phi_c^\infty} \approx 1 + \frac{3}{10} \left(2\pi \frac{v\tau}{H} \right) + \frac{1}{5} \left(2\pi \frac{v\tau}{H} \right)^2, \quad [4]$$

where v is the bacterial swimming speed and τ is the average duration between two tumble events (see SI Appendix). A similar equation was derived in (17), which explicitly takes

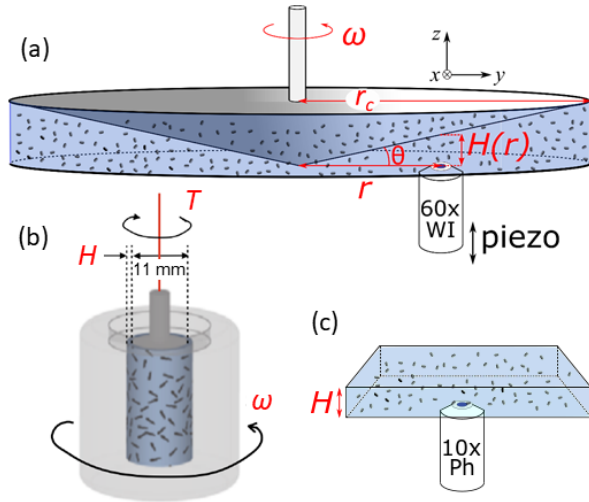


Fig. 2. Schematic of the three experimental setups used (not to scale): (a) Rheo-imaging setup using cone-plate geometry for visualisation during shear, (b) Couette cell for bulk rheometry; after (13) and (c) phase contrast imaging without applied shear.

into account wall-accumulation of bacteria. Figure 1 shows the predicted stability boundaries for $v = 15 \mu\text{m s}^{-1}$ and three values of τ (lines) using the experimental measured $\phi_c(H = 400 \mu\text{m}) \approx 0.75\%$ (see Results & Discussions) as ϕ_c^∞ . For $H \gtrsim 200 \mu\text{m}$, the CKT stability boundary is essentially flat, so that suspensions below $\phi_c \approx 0.75\%$ are predicted to be always stable. However, the calculated stability boundary turns sharply upwards at small H , so that at high confinement, very much higher cell densities are needed for the onset of collective motion.

Both ALCT and CKT predict $\eta(\phi)$ to be a decreasing function, i.e. NVI. Initial fitting of CKT to experimentally-measured $\eta(\phi)$ returns a microscopic length of $L \approx 20 \mu\text{m}$ for the bacterial force dipole (13), significantly larger than the $L \approx 2 \mu\text{m}$ inferred from experiments (33). To fit ALCT (18), one needs $K \sim 10 \text{ pN}$ at $\phi \lesssim 1\%$, which seems excessive in comparison to the $\approx 0.4 \text{ pN}$ (33) force scale of bacteria swimming. Nevertheless, both theories are consistent with the original qualitative picture: shear-induced alignment of either single dipoles (CKT) or putative local domains of nematicity-ordered swimmers (ALCT) activates the canonical NVI mechanism (8). To assess the soundness of the physical bases of these approaches therefore requires confrontation with fresh experiments probing directly size dependence. Such experiments would also help to establish a connection between the onset of collective motion and vanishing of the shear viscosity that was established theoretically (7, 17), but has never been verified experimentally. We now report such experiments.

Results & Discussions

Experimental details are given in Materials and Methods. Rheoimaging was performed using a cone-plate rheometer with bespoke optics for epi-fluorescence imaging (23), Fig. 2(a), while bulk rheometry was performed in a cylindrical (Couette) geometry with variable gap size, H (13), Fig. 2(b). Our cone-plate rheometer is not sensitive enough to determine the lower-than-water viscosities in NVI bacterial suspensions, but velocity profiles of the swimmers can be determined un-

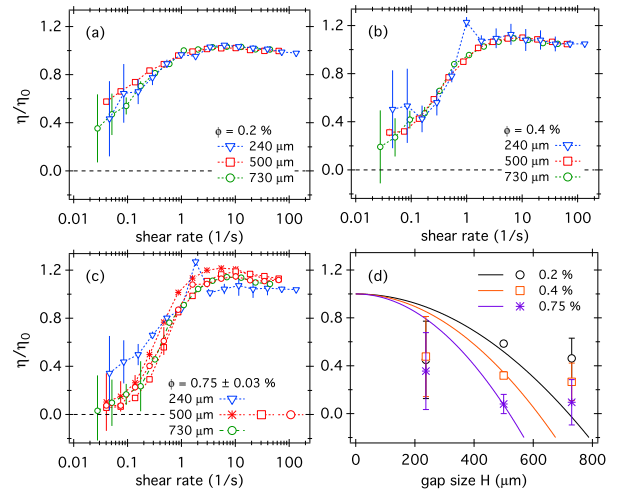


Fig. 3. The viscosity of *E. coli* suspensions as a function of shear rate, $\eta(\dot{\gamma})$, at gap sizes $H = 240, 500$ and $730 \mu\text{m}$ for $\phi =$ (a) 0.2% , (b) 0.4% , and (c) 0.75% . (d) The measured viscosity at $\dot{\gamma} \approx 0.04 \text{ s}^{-1}$ for three bacterial concentrations (symbols) compared to the predictions (color-matched) of ALCT (lines) using parameters from (18) and a cell volume $\mathcal{V}_B = 1.4 \mu\text{m}^3$ (34) and buffer viscosity $\eta_0 = 0.90 \text{ cP}$.

der conditions essentially identical to those used in Couette rheometry.

Before performing either Couette rheometry or rheoimaging, we always sealed $\approx 150 \mu\text{L}$ of the sample into $400 \mu\text{m}$ -high glass capillaries to monitor the onset of collective motion. Observations were carried out in a Nikon TE2000 inverted microscope with a PF 10 \times , N.A. 0.3 phase contrast objective, which allowed a large field of view ($\approx 700 \mu\text{m} \times 700 \mu\text{m}$). Movies were analyzed using Particle Image Velocimetry (PIV).

We used a fluorescent motility wild type strain of *E. coli*, AD21, dispersed in a minimal medium that prevented growth, but enabled motility for the time of the experiment (typically 0.5 h). Cell concentrations were determined by spectrophotometry and the relation between the measured optical density (OD) and cell number density was calibrated against cell counting. The corresponding volume fraction was calculated using a measured average cell body volume of $\mathcal{V}_B = 1.4 \mu\text{m}^3$ (34).

Size dependence of viscosity reduction. Figure 3 displays the viscosity of *E. coli* suspensions as a function of the shear rate $\dot{\gamma}$ for three different ϕ , each at three gap sizes, $H = 240, 500$ and $730 \mu\text{m}$. The $\eta(\dot{\gamma})$ data at the two higher bacterial densities are similar to those reported before (13) at $H = 500 \mu\text{m}$. At the lowest density, our apparatus could not reach the low-shear plateau. At all three cell densities, the viscosity data overlap over our range of gap sizes, $240 \leq H \leq 730 \mu\text{m}$. The predicted order-of-magnitude shift in $\dot{\gamma}_c$ between $H = 240 \mu\text{m}$ and $730 \mu\text{m}$, Eq. 1, is clearly absent, Fig. 3(a)-(c). The striking disagreement between ALCT and our data can also be brought out by comparing the measured and predicted viscosities at the lowest experimental shear rate, $\dot{\gamma} \approx 0.04 \text{ s}^{-1}$, Fig. 3(d). Although we cannot rule out weak size-dependence given the experimental noise, our results are inconsistent with the H^{-2} -dependence predicted by ALCT (18). Note that theory (lines) and experiments (symbols) agree at the single, previously-used, gap size of $H = 500 \mu\text{m}$, but clearly disagree at the other two gap sizes. This underlines the crucial importance of probing size dependence in theory-experiment comparisons.

We conclude that ALCT (18) is not applicable to bacteria suspensions at our cell densities. There is no evidence for *any* bending elasticity, let alone the strong elasticity ($K \sim 10$ pN) inferred by fitting to data at a single H (18).

Non-linear velocity gradients and collective motion. At $\dot{\gamma} \approx 0.04 \text{ s}^{-1}$, we find as before (13) that $\eta(\phi)$ decreases linearly for $H = 500 \mu\text{m}$, Fig. 4(a). Results for the other two gap sizes and additional shear rate values can be found in SI Appendix (Fig. S2). No significant systematic dependency with H is observed over the volume fraction range. At $\phi \gtrsim 0.75\%$, η remains approximately constant with ϕ . Irrespective of whether η actually reaches zero at $\phi \approx 0.75\%$, this density clearly marks the transition between two regimes. We probed this transition using rheoimaging, which yielded velocity profiles such as shown in Fig. 4(b-g).

At $\phi \lesssim 0.75\%$, velocity gradients are linear within experimental uncertainties. Above this density, pronounced non-linearities develop in the confinement gap. To quantify this transition, we calculated the standard deviations σ of $\Delta V_x(z) = V_x(z) - \dot{\gamma}_{\text{app}} z$ over the entire z range, where the applied shear rate was obtained from $\dot{\gamma}_{\text{app}} = V_x(z_{\text{cone}})/z_{\text{cone}}$, Fig. 4(h). Taken together, the data from five different experiments suggest that σ stays at a noise floor of ≈ 0.43 at low cell densities until $\phi \approx 0.75\%$, and then rises, consistent with where the density at which the low- η data extrapolates to zero. Importantly, visual inspection revealed large-scale correlated motions above this cell concentration. However, the small field of view in our setup ($\approx 180 \mu\text{m} \times 90 \mu\text{m}$) ruled out reliable PIV on our rheoimaging data sets.

Instead, we quantitatively analysed data from parallel imaging studies in sealed capillaries (no flow) and observed large-scale collective motion at $\phi \gtrsim 0.75\%$ manifested as vortices spanning a large fraction of the field of view, Fig. 4(i,j). We calculated the velocity correlation function,

$$c(r) = \left\langle \frac{\langle \vec{V}(\vec{r} + \vec{R}, t) \cdot \vec{V}(\vec{R}, t) \rangle_{\vec{R}} - \langle \vec{V}(\vec{R}, t) \rangle_{\vec{R}}^2}{\langle \vec{V}(\vec{R}, t) \rangle_{\vec{R}}^2 - \langle \vec{V}(\vec{R}, t) \rangle_{\vec{R}}^2} \right\rangle_t, \quad [5]$$

using PIV at various bacterial densities, where $\vec{V}(r)$ is the unit velocity vector at position \vec{r} , Fig. 4(k). A characteristic length-scale l for which $c(l) \approx 1/e$, Fig. 4(l), is extracted, which abruptly increases at $\phi \approx 0.75\%$, marking the onset of correlated motion.

Our rheoimaging setup was not sensitive enough to measure NVI directly. However, the flow profile at $\phi > 0.75\%$ measured in a cone-plate geometry is nearly flat near the stationary bottom plate, Fig. 4(c-g), which therefore experiences only small shear stress. This is further confirmed by the observation of a small but non-zero viscosity in the collective motion regime. Translated to the Couette cell used to measure bulk viscosities, this would be equivalent to null torque on the stationary inner cylinder and therefore a zero viscosity, corroborating the actual Couette rheometry finding of zero or very low viscosities at these concentrations, Fig. 4(a). We can therefore say with some confidence that the low-shear viscosity decreasing to zero at $\phi \approx 0.75\%$ appears to be correlated with the onset of non-linear velocity gradients *and* the emergence of large scale correlated motion Fig. 4(a,h,k).

Size dependence of collective motion. Our observation of a non-linear shear regime can be compared to a recent report

of ‘shear-banding’ by Guo *et al.* (15), which however was not accompanied by parallel visual observations and viscosity measurements, so that it is unclear whether their ‘banding’ is associated with either NVI or collective motion. If we nevertheless assume such association, then their results differ significantly from ours in one important quantitative respect. Guo *et al.* reported collective motion only at $\gtrsim 3.2 \times 10^{10}$ cells/ml, corresponding to $\phi \approx 4.5\%$ assuming $\mathcal{V}_b = 1.4 \mu\text{m}^3$, which is considerably higher than our critical concentration of $\phi_c \approx 0.75\%$. This discrepancy is likely due to system-size dependence: generally, Guo *et al.* worked at much higher confinement ($H = 60 \mu\text{m}$) than in our experiments.

Measurements of the bulk viscosity in our Couette cell display little size dependence in the range $240 \leq H \leq 730 \mu\text{m}$, Fig. 3. It was, however, not possible to decrease the gap size below $240 \mu\text{m}$ in this device. Observations at smaller gaps were, however, possible in our rheoimaging setup. Indeed, because we utilised a cone-plate geometry, shearing at a continuum of gap heights could be studied in a single experiment simply by moving the monitoring position radially. For $\phi \approx 1.5\%$, we observed strongly non-linear velocity gradients at $H \approx 200 \mu\text{m}$ and $H \approx 170 \mu\text{m}$, but linearity at $H \approx 100 \mu\text{m}$.

In Fig. 1 we compare the predicted CKT stability boundaries against our measurements. The threshold for $\tau = 2 \pm 0.5$ s credibly accounts for three data sets: our observation of the onset of collective motion in quiescent ($\dot{\gamma} = 0$) cell suspensions sealed in capillaries, our observation of the onset of non-linear flow profiles in cone-plate rheoimaging at $\dot{\gamma} = 0.04 \text{ s}^{-1}$, the observation by Guo *et al.* (15) of the onset of collective motion and of ‘banded’ states at $\dot{\gamma} = 0.16 \text{ s}^{-1}$.

Summary & Conclusions

To summarize, we have studied NVI, non-linear flow and collective motion in suspensions of motile *E. coli* bacteria at cell densities up to $\phi \lesssim 1.5\%$ using a combination of bulk rheometry, rheo-imaging, single-cell tracking and PIV. We find that the reduction of the bulk viscosity to zero at $\phi_c \approx 0.75\%$ coincides, within experimental accuracy, with the appearance of non-linear flow and the onset of collective motion when the swimmers are confined to a gap in the range $170 \leq H \leq 730 \mu\text{m}$. The independence of the measured viscosity with gap H rules out the applicability of ALCT (18) to bacterial suspensions of this kind, showing that the nematic orientational elasticity assumed in this treatment is absent. The stability boundary for sheared *E. coli* suspensions within a CKT framework is shown to be consistent with our observations of the onset of collective motion and non-linear velocity gradients in the range $100 \leq H \leq 400 \mu\text{m}$ as well as recent observations at the even higher confinement of $H = 60 \mu\text{m}$ (15).

This success of CKT prompts us to revisit a previous comparison of this theory with NVI experiment (13), which found that fitting $\eta(\phi)$ data to this theory required a dipolar length for the pushers that was an order of magnitude larger than the experimental value. The source of this discrepancy lies in the fact that the version of CKT used in this comparison (27) was for swimmers whose swimming direction decorrelates due to rotational Brownian motion, while the swimmers used in the corresponding experiments (and in this work) are run-and-tumblers that decorrelate due to sudden directional changes. A comparison taking this into account fits our data.

Our work demonstrates an intimate relationship between

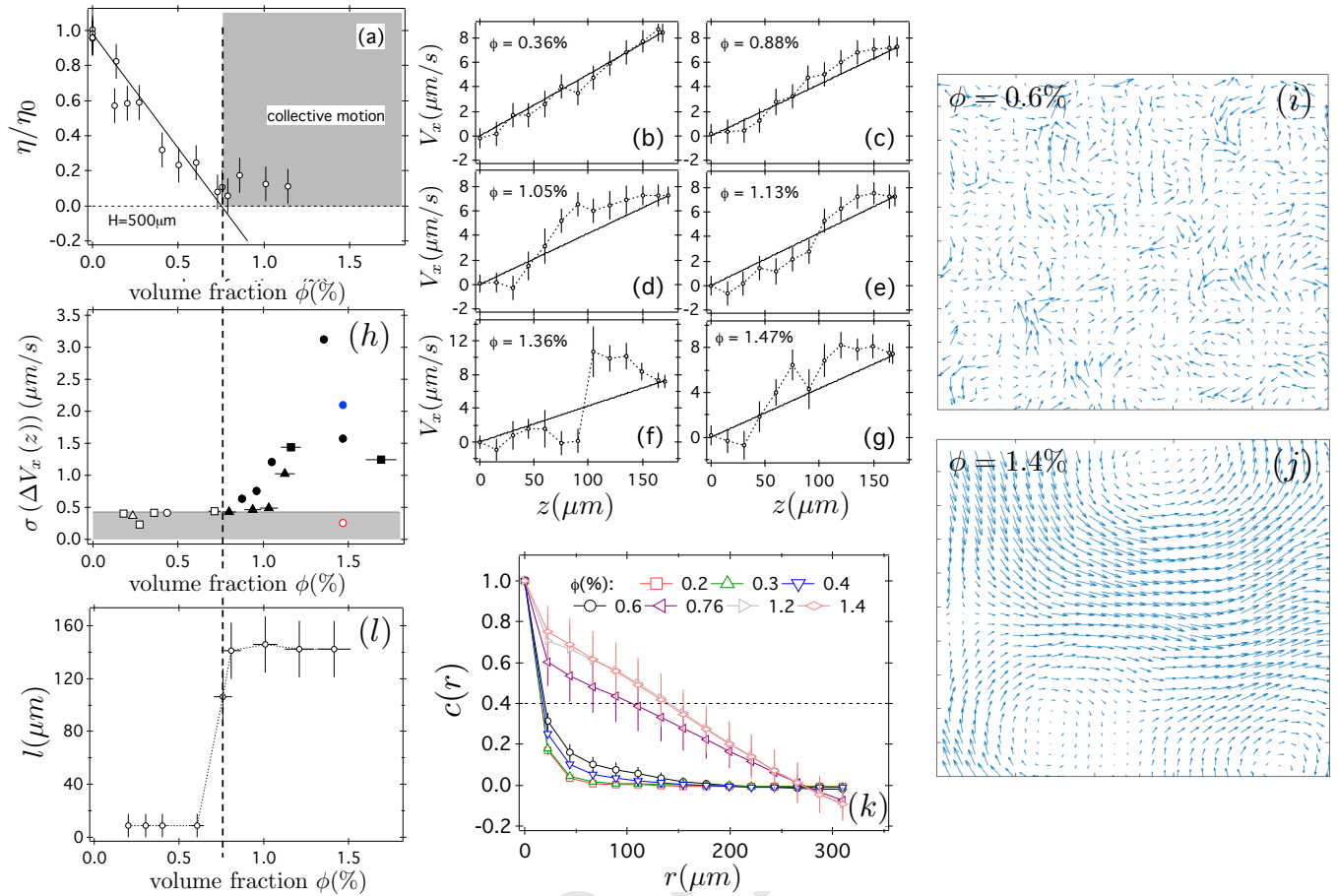


Fig. 4. (a) The viscosity of *E. coli* suspensions measured with a gap $H = 500 \mu\text{m}$ at a shear rate $\dot{\gamma} \approx 0.04 \text{ s}^{-1}$, as a function of volume fraction, normalised to the viscosity of the buffer $\eta_0(c_{\text{serine}}) = (0.87 + 2.7 \times 10^{-4} c_{\text{serine}}) \text{ cP}$, with c_{serine} the concentration of serine used to prepare the solutions. The grey area defines the presence of large-scale collective motion, observed above $\phi_c \approx 0.75\%$ (vertical dashed line), as characterised in Fig. 4(i-l). (b-g) Examples of velocity profiles measured using rheoimaging in cone-plate geometry of bacterial suspensions at progressively higher volume fraction ϕ , as indicated, and for $\dot{\gamma} \approx 0.04 \text{ s}^{-1}$ and $H = 170 \mu\text{m}$. (h) Standard deviation σ of $\Delta V_x(z) = V_x(z) - \dot{\gamma}_{\text{app}} z$ over the entire z range, with the applied shear rate $\dot{\gamma}_{\text{app}} = V_x(z_{\text{cone}})/z_{\text{cone}}$, as a function of volume fraction. Open and filled symbols indicate linear and non-linear flow profile, respectively, for $H = 100 \mu\text{m}$ (red), $170 \mu\text{m}$ (black, each symbol corresponds to an independent experimental campaign), and $200 \mu\text{m}$ (blue). Grey area defines the linear flow range based on an arbitrary threshold of $\sigma \lesssim 0.43$. (i,j) Examples of velocity vectors from PIV at two ϕ (i) below and (j) above $\phi_c \approx 0.75\%$. Image width is $\approx 700 \mu\text{m}$. (k) Velocity correlation functions $c(r)$ calculated from Eq. 5 and averaged over $5 \lesssim t \lesssim 15 \text{ min}$ at various ϕ measured via PIV analysis of phase-contrast microscopy videos of cell suspensions in sealed capillaries with $H = 400 \mu\text{m}$. Error bars are \pm one standard deviation representative of the time-dependency. (l) Characteristic length $l(\phi)$ for which $c(l, \phi) \approx 1/e$.

the onset of collective motion and vanishing of the viscosity. It has previously been shown (17, 35–37) that collective motion is very sensitive to the geometry of the system. Future work is required to establish whether the relationship reported in this work holds in the general case.

Taken together, our experiments show that the emergence of ‘superfluidity’ in bacterial suspensions is correlated with the onset of non-linear flow and collective motion, and that CKT is able to explain the magnitude of NVI as well as the system size dependence of flow instabilities. These findings demonstrate the value of performing bulk and single-cell measurements in parallel in studying some of the most striking phenomena in active matter.

Materials and Methods

Bacteria growth protocol. We cultured a strain of *E. coli* K12 derived from AB1157, which we have described previously (38). Here we have further modified this strain, now called AD21, to include a

plasmid which expresses yellow fluorescent protein (YFP), therefore all growth media were supplemented with chloramphenicol ($25 \mu\text{g ml}^{-1}$). Briefly, an overnight culture of AD21 was obtained by inoculating a single colony into 10 mL of LB followed by incubation at $30^\circ\text{C}/200 \text{ rpm}$ for 16–18 h. Next day this was inoculated into 35 mL of TB medium (1:100 dilution) which was incubated for 4 h ($30^\circ\text{C}/200 \text{ rpm}$) to obtain a late exponential phase culture. At this stage cells were harvested and concentrated by gentle filtration ($0.45 \mu\text{m}$ HATF filter; Millipore). This concentrated culture was washed by successive resuspension into 35 mL of motility buffer (MB, pH = 7.0, 6.2 mM K_2HPO_4 , 3.8 mM KH_2PO_4 , 67 mM NaCl, and 0.1 mM EDTA) followed by filtration from one to three times to yield 1–2 mL of cells at high density $\phi \approx 1.0$ – 1.5% . Suspensions at different ϕ were prepared with MB supplemented, prior to experiments, with serine in the range 20–150 mM depending on ϕ to promote anaerobic motility. To some experiments, we added dialyzed polyvinylpyrrolidone (0.01%w, molecular weight 360k, Sigma Aldrich) to prevent cell adhesion to surfaces but did not observe significant changes than without. Suspensions with a volume of $\approx 400 \mu\text{L}$, $\approx 1 \text{ mL}$, and $\approx 150 \mu\text{L}$ were then used for rheoimaging (Edinburgh), bulk rheology (Orsay), and phase-contrast imaging (both), respectively. Volume fractions ϕ were obtained by converting measurement of optical densities (OD) using a range of spectrophotometers, and assuming

a bacterium volume $V_B = 1.4 \mu\text{m}^3$ (34). Each spectrophotometer was calibrated based on viable plate count (38). Additionally, we monitored, in some cases, the time-dependency of bacterial motility by measuring the swimming speed using Differential Dynamic Microscopy (38, 39). This allowed us to define an experimental time window of ≈ 30 min over which motility is approximately constant for the densest suspensions.

Bulk rheometry. Experiments were carried out in a cylindrical low-shear Couette geometry (13), Fig. 2(b). An inner cup (radius $R_i = 5.5$ mm) is suspended by a torsion wire inside an outer cup of radius $R_o = R_i + H$ ($H = 240, 500$ and $730 \mu\text{m}$). The latter rotates with speed ω , setting the shear rate $\dot{\gamma}$. The torque T needed to keep the inner cylinder stationary is measured and converted into stress. The ratio gives the viscosity η , which is therefore a surrogate for the stress at the inner cylinder.

To obtain the viscosity plots in Figure 3, we used the same protocol as in (13). The outer cup was first filled with a small volume of the suspension (~ 1 mL), and then the inner cup was set into place. After 30 s of rest, the inner cup was rotated for 30 s at a steady state shear rate. The rotation was then stopped for 30 s. For some of the measurements performed with the highest concentrations, the steps were maintained for 60 s for the lowest shear rates. These steps were repeated with increasing shear rate values. We have improved our previous data analysis procedure (13). The signals were automatically analysed by a routine implemented in Matlab. The average viscosity during one measurement was obtained by removing the zero shear baseline measured from a linear fit based on the instrumental signal obtained before and after the corresponding applied shear. The error bars in Fig. 3 correspond to the root-mean-square values of the signal for each independent measurements. The error bars in fig. 4 represent the reproducibility of measurements performed at the same bacterial concentration but for different experimental campaigns, i.e. different days and bacterial batch suspensions, and thus include variability in suspension activity and rheometer settings (e.g. apparatus alignment is performed manually).

Rheoimaging. Experiments were performed using a cone-plate geometry, Fig. 2(a), ($\theta = 1^\circ$, radius $r_c = 20$ mm) connected to an AR2000 rheometer (TA Instruments) (23), with bespoke optics for epi-fluorescence imaging. In this set-up, the resulting torques are too weak to determine the suspension viscosity, however the bacteria velocity profiles can be determined in conditions essentially similar to the bulk rheometry measurements.

The sample was imaged through a microscope coverslip serving as the bottom plate using a custom build imaging module in epi-fluorescence mode (see Fig. 2 for a schematic). The imaging module consists of a blue LED (M470L2, Thorlabs), a GFP filter cube (LED-FITC-A, Semrock), a water immersion objective (PA60x/1.2 WI, Nikon) and a fast and sensitive CMOS camera (Orca Flash 4.0, Hamamatsu). It can be focused at different heights within the sample using a piezo objective mount (P-725.4CD, PI) and moved manually to well defined radial positions relative to the rotation axis. Extra care was taken to avoid bending the bottom coverslip while loading the sample and the sample was sealed off with a home-build enclosure to minimise solvent evaporation.

We mostly worked ≈ 10 mm away from the rotation axis, where we can monitor the entire height ($\approx 170 \mu\text{m}$) of the sample, and recorded $180 \mu\text{m} \times 90 \mu\text{m}$ movies of 2000 frames at 400 fps or 1000 frames at 100 fps at various heights at a step size of $\Delta z = 15 \mu\text{m}$. Cell bodies showed up as bright features and 2D tracks, in the focal, or (x, y) , plane were extracted using Trackmate (ImageJ) (40). The 100-1000 tracks in each data set remaining in the (x, y) plane for longer than 0.1 s were extracted. Velocities along the x and y axes are measured by deriving smoothed trajectories (smoothing over 0.1 s using a third-order Savitzky-Golay filter).

Particle Image Velocimetry. We recorded phase-contrast movies (≈ 40 s-long, $\text{PF } 10\times$, N.A. 0.3) with large field of view ($\approx 700 \mu\text{m} \times 700 \mu\text{m}$) near the middle of a $400 \mu\text{m}$ -height capillary to avoid wall effect. Approximately 10 to 15 movies were recorded over a period of ≈ 15 min shortly after adding the serine, filling and sealing the capillary. Each movie was analysed independently with PIV yielding one velocity correlation function per movie. We found no systematic

time-dependency of these correlation functions and thus we averaged these together. The error bars presented in Figure 4k represent \pm one standard deviation. We used a standard Matlab Particle image velocimetry software adapted from the PIVLab toolbox (41, 42). The time scale between two successive images is 0.2 s (20 frames). The final metapixel box is $32 \times 32 \text{ pix}^2$ ($\approx 42 \times 42 \mu\text{m}^2$) with an initial half-box size spatial shift. Non-motile fraction of the bacterial solutions was negligible ($\lesssim 10\%$) and thus PIV analysis was mostly based on motion of motile cells.

Data availability

The research data underpinning this publication will be available on the Edinburgh DataShare repository and a DOI link will be added if the paper is accepted.

ACKNOWLEDGMENTS. The work was funded by CNRS/Royal-Society (PHC-1576 and IE160675), the European Research Council (AdG 340877-PHYSAPS), the EU-FP7-infrastructures 'ESMI' (CP & CSA-2010-262348) and ANR-15-CE30-0013 'Bacflow' Grant. We thank Christophe Manquest for technical support for viscosity measurements.

- Poon WCK (2013) From *Clarkia* to *Escherichia* and Janus: The physics of natural and synthetic active colloids in *Physics of Complex Colloids*, eds. Bechinger C, Sciortino F, Zilber P. (Società Italiana di Fisica, Bologna), pp. 317–386.
- Cates ME (2012) Diffusive transport without detailed balance in motile bacteria: does microbiology need statistical physics? *Rep. Prog. Phys.* 75:042601.
- Arit J, Martinez VA, Dawson A, Pilizota T, Poon WCK (2019) Dynamics-dependent density distribution in active suspensions. *Nature Communications* 10(2019):2321.
- Lauga E, Powers TR (2009) The hydrodynamics of swimming microorganisms. *Rep. Prog. Phys.* 72:096601.
- Ramaswamy S (2010) The mechanics and statistics of active matter. *Annu. Rev. Condens. Matter Phys.* 1:323–345.
- Ezhilan B, Shelley MJ, Saintillan D (2013) Instabilities and nonlinear dynamics of concentrated active suspensions. *Phys. Fluids* 25:070607.
- Subramanian G, Koch DL (2009) Critical bacterial concentration for the onset of collective swimming. *Journal of Fluid Mechanics* 632:359–400.
- Hatwalne YV, Ramaswamy S, Rao M, Simha RA (2004) Rheology of active-particle suspensions. *Phys. Rev. Lett.* 92:118101.
- Rafai S, Peyla P, Jibuti L (2010) Effective viscosity of microswimmer suspensions. *Phys. Rev. Lett.* 104:098102.
- Sokolov A, Aranson IS (2009) Reduction of viscosity in suspension of swimming bacteria. *Phys. Rev. Lett.* 103:148101.
- Gachelin J, et al. (2013) Non-newtonian viscosity of *escherichia coli* suspensions. *Phys. Rev. Lett.* 110(26):268103.
- Liu Z, Zhang K, Cheng X (2019) Rheology of bacterial suspensions under confinement. *Rheologica Acta*.
- López HM, Gachelin J, Douarche C, Auradou H, Clément E (2015) Turning bacteria suspensions into superfluids. *Phys. Rev. Lett.* 115(2):028301.
- Saintillan D (2018) Rheology of active fluids. *Annual Review of Fluid Mechanics* 50(1):563–592.
- Guo S, Samanta D, Peng Y, Xu X, Cheng X (2018) Symmetric shear banding and swarming vortices in bacterial superfluids. *Proc. Natl. Acad. Sci. (USA)* 115(28):7212–7217.
- Hohenegger C, Shelley MJ (2010) Stability of active suspensions. *Phys. Rev. E* 81:046311.
- Theillard M, Alonso-Matilla R, Saintillan D (2017) Geometric control of active collective motion. *Soft Matter* 13(2):363–375.
- Loisy A, Eggers J, Liverpool TB (2018) Active suspensions have nonmonotonic flow curves and multiple mechanical equilibria. *Phys. Rev. Lett.* 121(1):018001.
- Binder K (2003) Overcoming the limitation of finite size in simulations: From the phase transition of the Ising model to polymers, spin glasses, etc. *AIP Conf. Proc.* 690(1):74–84.
- Napolitano S, Glynnos E, Tito NB (2017) Glass transition of polymers in bulk, confined geometries, and near interfaces. *Rep. Prog. Phys.* 80:036602.
- Zumaya M, Larraalde H, Aldana M (2018) Delay in the dispersal of flocks moving in unbounded space using long-range interactions. *Sci. Rep.* 8:15872.
- Marchetti MC, et al. (2014) Hydrodynamics of soft active matter. *Rev. Mod. Phys.* 85:1143.
- Besseling R, Isa L, Weeks ER, Poon WC (2009) Quantitative imaging of colloidal flows. *Adv. Colloid Interface Sci.* 146:1–17.
- Sanchez T, Chen DTN, DeCamp SJ, Heymann M, Dogic Z (2012) Spontaneous motion in hierarchically assembled active matter. *Nature* 491:431–435.
- Aditi Simha R, Ramaswamy S (2002) Hydrodynamic fluctuations and instabilities in ordered suspensions of self-propelled particles. *Phys. Rev. Lett.* 89(5):058101.
- Haines BM, Sokolov A, Aranson IS, Berlyand L, Karpeev DA (2009) Three-dimensional model for the effective viscosity of bacterial suspensions. *Phys. Rev. E* 80(4):041922.
- Saintillan D (2010) The dilute rheology of swimming suspensions: A simple kinetic model. *Exp. Mech.* 50:1275–1281.
- Beris A, Edwards B (1994) *Thermodynamics of Flowing Systems with Internal Microstructure*. (Oxford University Press).
- de Gennes PG, Prost J (1995) *The Physics of Liquid Crystals*. (Clarendon Press).
- Stenhammar J, Nardini C, Nash RW, Marenduzzo D, Morozov A (2017) Role of correlations in the collective behavior of microswimmer suspensions. *Phys. Rev. Lett.* 119(2):028005.

- 518 31. Koessel, Fabian R., Jabbari-Farouji, Sara (2019) Controlling stability and transport of mag-
519 netic microswimmers by an external field. *EPL* 125(2):28001.
- 520 32. Guzmán M, Soto R (2019) Nonideal rheology of semidilute bacterial suspensions. *Phys. Rev.*
521 *E* 99(1):012613.
- 522 33. Drescher K, Dunkel J, Cisneros LH, Ganguly S, Goldstein RE (2011) Fluid dynamics
523 and noise in bacterial cell–cell and cell–surface scattering. *Proc. Natl. Acad. Sci. (USA)*
524 108(27):10940–10945.
- 525 34. Jepson A, Martinez VA, Schwarz-Linek J, Morozov A, Poon WCK (2013) Enhanced diffusion
526 of nonswimmers in a three-dimensional bath of motile bacteria. *Phys. Rev. E* 88:041002(R).
- 527 35. Wioland H, Woodhouse FG, Dunkel J, Kessler JO, Goldstein RE (2013) Confinement stabi-
528 lizes a bacterial suspension into a spiral vortex. *Phys. Rev. Lett.* 110(26):268102.
- 529 36. Wioland H, Lushi E, Goldstein RE (2016) Directed collective motion of bacteria under channel
530 confinement. *New Journal of Physics* 18(7):075002.
- 531 37. Beppu K, et al. (2017) Geometry-driven collective ordering of bacterial vortices. *Soft Matter*
532 13(29):5038–5043.
- 533 38. Schwarz-Linek J, et al. (2016) *Escherichia coli* as a model active colloid: A practical introduc-
534 tion. *Colloids Surf. B* 137:2–16.
- 535 39. Martinez VA, et al. (2012) Differential dynamic microscopy: a high-throughput method for
536 characterizing the motility of microorganisms. *Biophys. J.* 103:1637–1647.
- 537 40. Schindelin J, et al. (2016) TrackMate: An open and extensible platform for single-particle
538 tracking. *Methods* 115:80–90.
- 539 41. Thielicke W, Stamhuis E (2014) Pivlab - towards user-friendly, affordable and accurate digital
540 particle image velocimetry in matlab. *Journal of Open Research Software* 2(1):e30.
- 541 42. Thielicke W, Stamhuis E (2014) Pivlab - time-resolved digital particle image velocimetry tool
542 for matlab (version: 2.00). *Journal of Open Research Software*.

DRAFT